RSC Advances

ROYAL SOCIETY OF CHEMISTRY

www.rsc.org/advances

Graphical Abstract

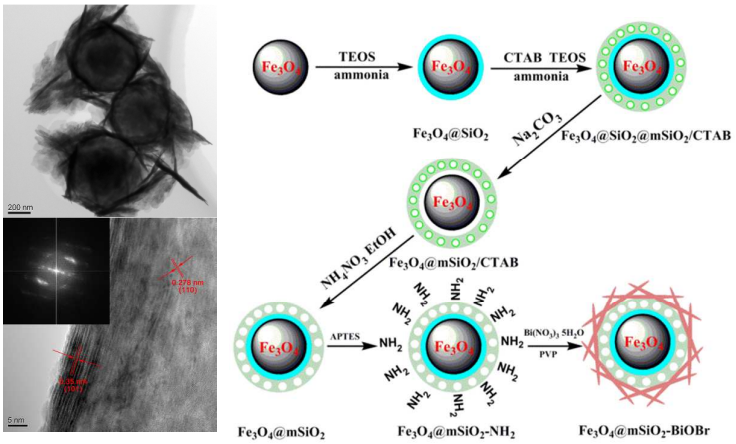

The rattle-type Fe_3O_4@mSiO_2@BiOBr photocatalyst, which is a superior alternative visible-light-driven photocatalyst, was successfully synthesized.

[1]Synthesis of rattle-type magnetic mesoporous Fe_3O_4@mSiO_2@BiOBr hierarchical photocatalyst and its photoactivity investigation in degradation of methylene blue

Wei Li,[a,b] Yi Tian,[a,b] Peitao Li,[a,b] Baoliang Zhang,[a,b] Hepeng Zhang,[a,b] Wangchang Geng,*[a,b] Qiuyu Zhang*[a,b]

[a]Department of Applied Chemistry, College of Science, Northwestern Polytechnical University, Xi'an 710072, China

[b]Key Laboratory of Space Physics and Chemistry, Ministry of Education, Northwestern Polytechnical University, P. O. Box 624, Xi'an 710072, China

Abstract: The rattle-type magnetic mesoporous Fe_3O_4@mSiO_2@BiOBr hierarchical photocatalyst was successfully synthesized by a facile solvothermal synthesis under the orientation of the surface amino-groups of rattle-type magnetic mesoporous Fe_3O_4@mSiO_2 microspheres, then this photocatalyst was characterized via X-ray diffraction, transmission electron microscopy, field-emitting scanning electron microscope, fourier transform-infrared spectra, X-ray photoelectron spectroscopy and vibrating sample magnetometer, respectively. Due to the presence of inner cavity and orderly mesoporous opening structure, this novel photocatalyst exhibits superior adsorption and transfer performance to organic contaminants in water system. Especially, the complex between BiOBr and SiO_2 had significantly increased the absorption ability to visible-light to some extent for the direct contact of the interfaces of two materials. Research shows that the assembly capacity of BiOBr nanosheets plays an important role to the enhanced photoactivity. Even though methylene blue is a relatively stable organic contaminant, it can still be decomposed completely by this novel photocatalyst in a very short time (about 120 min). Encouragingly, the photoactivity of this novel photocatalyst is far higher (about 2.6 times) than that of pure BiOBr photocatalyst for its unique structure. According to the radical trapping experiments, the photogenerated holes (h+) and superoxide radicals ($O_2^{\bullet-}$) were considered as the main active species to drive the photodegradation under visible-light irradiation. For the unique structures and fast interfacial charge transfer, this novel photocatalyst absolutely is a superior alternative visible-light-driven photocatalyst.

[1] Corresponding author: Fax: +86-029-88431675 E-mail: qyzhang@nwpu.edu.cn (Qiuyu Zhang), w.geng@nwpu.edu.cn (Wangchang Geng)

Keywords: photocatalysis; magnetic response; mesoporous silica; heterogeneous catalysis; visible-light irradiation

1. Introduction

Semiconductor photocatalysis technique is an effective method to eliminate most kinds of environmental contaminations and produce hydrogen.[1-5] Among the various semiconductor photocatalysts, bismuth oxyhalides are extensively investigated in recent years due to their superior properties and potential applications. For the favourable visible-light absorption ability of most of bismuth oxyhalides, these photocatalysts had been studied in varying degrees by many researchers. For instance, Weng et al.[6] reported that single-crystalline BiOCl nanosheets exposing (010) facets exhibit higher photoactivity due to more surface complex and more terminal bismuth atoms on the surface of BiOCl (010). Shi et al.[7] fabricated a BiOBr hierarchical nanostructures by polyvinyl pyrrolidone (PVP) assisted hydrothermal method. They found that the concentration of PVP in the reaction mixture played a key role on controlling structures and morphologies because PVP could attach on the (012) plane of the BiOBr hierarchical nanostructures selectively and insulate the growth of this plane. However, as a semiconductor with a wide band gap, the absorption ability of pure bismuth oxyhalides to visible-light is very limited for degrading organic contaminants in water system. Hence, many efforts have been devoted to develop functional bismuth oxyhalides based visible-light photocatalysts by incorporating metal ions or coupling with other semiconductors. For instance, Yu et al.[8] prepared the noble metal (Rh, Pd, Pt)/BiOX(Cl, Br, I) composite photocatalysts, and their study showed that appropriate noble metal depositions can effectively enhance the visible-light absorption and photoactivity of bismuth oxyhalides based photocatalyst for the promoted separation rate of photogenerated electron-hole pairs and the role of plasmon photocatalysis. Furthermore, Jiang et al.[9] prepared the visible-light-induced BiOBr photocatalysts by chemical reduction, photoreduction and thermal reduction, respectively. They thought the solvothermal reduction method was relatively simple and efficient, and the 3% Ag/Ti-doped BiOBr photocatalysts exhibited the higher photoactivity and excellent durability. Beyond that, Wei et al.[10] prepared an BiOBr-TiO_2-graphene composite, and this material also exhibited superior photoactivity towards the photodegradation of rhodamine B under visible-light irradiation.

To effective improve the separation of the photocatalyst, preparing the photocatalyst with

appropriate particle size or good magnetic response is the most effective method. Especially, the good magnetic response can fulfill the simple magnetic separation and regeneration of the photocatalyst. For instance, Zhang et al.[11] prepared a magnetic BiOBr@SiO_2@Fe_3O_4 photocatalyst, and their research revealed that this recyclable magnetic photocatalyst exhibited more superior photoactivity than that of commercial TiO_2 under visible-light irradiation. Furthermore, Guo et al.[12] prepared a plasmonic photocatalyst of Ag-AgI/Fe_3O_4@SiO_2 by deposition-precipitation and photoreduction method, and this photocatalyst exhibited efficient photoactivity for the degradation of rhodamine B and 4-chlorophenol and could be easily recovered due to its paramagnetic property.

Beyond that, the superior adsorption ability of the photocatalyst to organic contaminant molecules is also an important role to its degradation performance. To the best of our knowledge, mesoporous silica shows very high specific surface area for its orderly mesoporous opening structure.[13,14] Combining the mesoporous structure with rattle-type structure undoubtedly can improve the mass transport ability significantly for presence of the inner cavities and the connected mesopores, and it can indirectly enhance the degradation ability to some extent. Based on this idea, we designed and synthesized a novel rattle-type magnetic mesoporous Fe_3O_4@mSiO_2@BiOBr hierarchical photocatalyst by a facile solvothermal synthesis under the orientation of the surface amino-groups of rattle-type magnetic Fe_3O_4@mSiO_2 microspheres. For the presence of inner cavity and orderly mesoporous opening structure, this hierarchical photocatalyst exhibited very high adsorption ability to organic contaminant molecules. Simultaneously, for the direct contact between BiOBr semiconductor and mesoporous silica, it can effective improve the interfacial charge transfer and enhance the suppression of the rapid recombination of photogenerated electron-hole pairs, thus this novel rattle-type magnetic mesoporous Fe_3O_4@mSiO_2@BiOBr hierarchical photocatalyst exhibited very superior photoactivity for degradation of methylene blue in water system. At the same time, the main active species were also investigated by the radical trapping experiments, and the h^+ and $O_2^{\bullet-}$ radicals were demonstrated to be the main active species to drive the photodegradation under the irradiation of visible-light.

2. Experimental Section

2.1. Reagents and Materials. All chemicals were purchased from J & K Chemical and were used without further treatment.

2.2. Preparation of Rattle-Type Magnetic Mesoporous Fe_3O_4@$mSiO_2$ Microspheres. The magnetic mesoporous Fe_3O_4@SiO_2@$mSiO_2$/CTAB microspheres with double shell structure were prepared by optimizing our previous method[15]. Subsequently, the rattle-type magnetic mesoporous Fe_3O_4@$mSiO_2$/CTAB composite microspheres were successfully synthesized after the etching process at the presence of CTAB. Briefly, 5 g of dried aforementioned microspheres was redispersed into 500 mL of distilled water. After being treated by ultrasonic for 15 min, 10 g of anhydrous Na_2CO_3 was added into this system, and the reaction system was stirred vigorously for 10 h at 50℃. After the reaction finished, the sample was separated from the system by applying an external magnetic field, and was washed several times with distilled water with the aid of ultrasonic technique. Lastly, the ultimate sample was dried for 12 h via the vacuum freeze-drying technology. Here, it was expressed as R-Fe_3O_4@$mSiO_2$.

2.3. Preparation of Rattle-Type Magnetic Mesoporous Fe_3O_4@$mSiO_2$@BiOBr Hierarchical Photocatalyst. The aforementioned R-Fe_3O_4@$mSiO_2$ microspheres were firstly modified with γ-aminopropyltriethoxysilane (APTES), then BiOBr sheets were orientablly assembled on the surface of this composite material through the complexation between the amino-groups and Bi^{3+} ions. Briefly, 1.5 g of rattle-type magnetic mesoporous Fe_3O_4@$mSiO_2$ microspheres was ultrasonically dispersed into 200 mL of acetone, and 4-6 drops of ammonia solution (25 wt%) was added, then the system was stirred vigorously for 15 min. Subsequently, the temperature was adjusted to 60℃, and 4 mL of APTES was added into aforementioned system, then this system was stirred for 12 h at the speed of 250 rpm. After the reaction finished, the sample was collected from the system by applying an external magnetic field and washed several times with acetone and distilled water, respectively. Ultimately, the sample was dried for 12 h via the vacuum freeze-drying technology, and the amino-functionalized rattle-type magnetic mesoporous silica microspheres (R-Fe_3O_4@$mSiO_2$-NH_2) were successfully obtained. Then, 0.3 g of R-Fe_3O_4@$mSiO_2$-NH_2, 0.5 g of KBr, 0.1 g of PVP and different stoichiometric $Bi(NO_3)_3 \cdot 5H_2O$ were added into 40 mL of EG, then this system was treated for 15 min under ultrasound to form a uniform dispersed system. Afterwards, aforementioned suspension was transfered to a teflon-lined stainless steel autoclave with a capacity of 50 mL and kept for 8 h at 180℃. After the reaction finished, the system was naturally cooled to room temperature, then the sample was separated by applying a permanent magnet externally and washed several times with ethanol and distilled water, respectively. Lastly, the sample was dried for 12 h via

the vacuum freeze-drying technology, and the ultimate product was successfully obtained. Beyond that, the samples prepared under different temperature or reaction time were also obtained by aforementioned method, and the sample prepared at the absence of PVP was also prepared by the same method. Here, it was expressed as R-Fe_3O_4@mSiO_2@BiOBr-α-β (α = 0, 0.2, 0.4, 0.6, 0.8 and 1.0 g, and β = 2, 4 and 6 h).

2.4. Characterization. Fourier transform-infrared (FT-IR) spectra of the samples were recorded on a Perkin-Elmer 580BIR spectrophotometer using the KBr pellet technique. X-ray powder diffraction (XRD) analysis was performed on a Bruker AXS D8-advance X-ray diffractometer with Cu Kα radiation. The morphologies and sizes of the samples were characterized using the transmission electron microscopy (TEM, JEOL JEL2010) and field-emitting scanning electron microscope (FESEM, JEOL-JSM-6700 F). X-ray photoelectron spectroscopy (XPS) datas were collected to examine the chemical states of the multi-component photocatalyst with an Axis Ultra instrument (Kratos Analytical, Manchester, U.K.) under ultrahigh vacuum condition (<10^{-6} Pa) and using a monochromatic Al Kα X-ray source (1486.6 eV). N_2 adsorption/desorption isotherms were obtained on a TriStar II 20 apparatus. The Brunauer-Emmett-Teller (BET) method was used to calculate the specific surface area based on the adsorption branches.

2.5. Photocatalytic performance tests. The photocatalytic activities of the as-prepared R-Fe_3O_4@mSiO_2@BiOBr hierarchical photocatalysts were evaluated by catalyzing the photodegradation of MB in water system at room temperature under the visible light irradiation with one 500 W xenon lamp (CHF-XM500, light intensity = 600 mW/cm^2) located at 20 cm away from the reaction solution. To make sure that the photocatalytic reaction was really driven by visible-light, all the UV lights with the wavelength less than 420 nm were removed by a glass filter (JB-420). In a typical reaction, 0.1 g of as-prepared photocatalyst was dispersed into 100 mL of MB aqueous solution (20 mg/L). Before the light irradiation, the suspension was stirred for 30 min in dark to reach the saturated adsorption equilibrium of MB molecules. Then, 5 mL of degradation solution was extracted to determine the concentration of the MB in aqueous solution by UV-vis spectroscopy. In this study, the pure BiOBr photocatalyst was also used as the reference catalyst to catalyze the photodegradation of MB under the same condition as aforementioned operation. The MB aqueous solution without photocatalyst irradiated by visible light was used as the blank experiment. After the experiment was finished, the catalyst was collected by centrifugal separation and washed several

times with ethanol and distilled water, respectively. Then, the photodegradation experiment catalyzed by the recovered catalyst was carried out repeatedly according to aforementioned operation steps.

2.6. Radical Trapping Experiments. For detecting the main active species during photocatalytic reactivity, holes (h^+), photoexcited electrons (e^-), hydroxyl radicals (•*OH*) and superoxide radical (O_2•-) were investigated by adding 1.0 mM KI (a scavenger of photogenerated h^+)[16], 1.0 mM tert-butanol (TBA, a quencher of photoexcited e^-)[17], 1.0 mM isopropanol (IPA, a scavenger of •*OH*)[18], and 1.0 mM 1,4-benzoquinone (BQ, a scavenger of O_2•-)[19], respectively. The method was similar to the former photocatalytic activity test.

3. Results and Discussion

3.1. Characterization of Materials

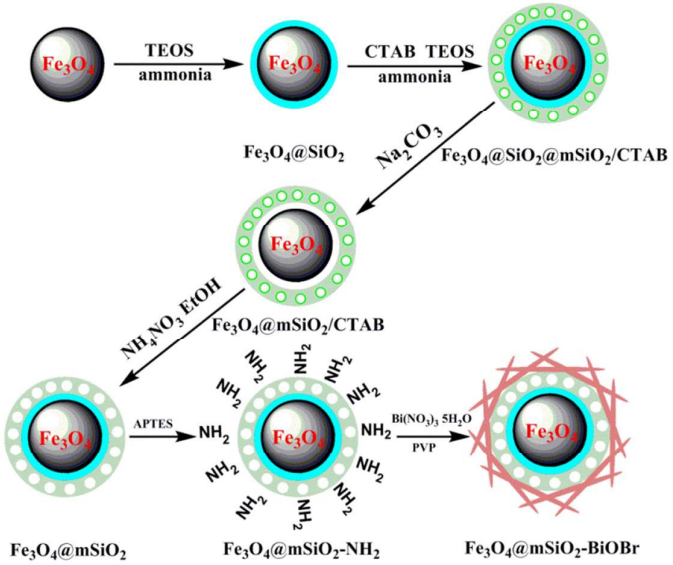

Fig.1 Schematic illustration of the synthesis of the magnetic R-Fe_3O_4@$mSiO_2$-BiOBr photocatalyst.

The synthesis of the magnetic R-Fe_3O_4@$mSiO_2$-BiOBr photocatalyst was depicted in Fig.1. To investigate the morphologies of Fe_3O_4, Fe_3O_4@SiO_2, Fe_3O_4@SiO_2@$mSiO_2$ and R-Fe_3O_4@$mSiO_2$, TEM characterization was carried out, and Fig.2 displays the corresponding TEM images. The magnetic Fe_3O_4 microparticles synthesized by the solvothermal synthesis show representative cauliflower-like morphology, and its diameter is about 500 nm (as Fig.2**a** and Fig.2**b**). After being coated with a layer of dense silica film, the surface of the particles becomes more smooth than that of Fe_3O_4, and the representative core-shell structure with the shell thickness of 35 nm can be observed clearly (as Fig.**2**c and Fig.2**d**). Subsequently, the magnetic mesoporous Fe_3O_4@SiO_2@$mSiO_2$/CTAB

microspheres with double-shell structure were successfully obtained, and the thickness of the outer mesoporous silica coating is about 50 nm (as Fig.2**e** and Fig.2**f**). After the etching process, the internal dense silica coating was successfully removed under the protection of CTAB, and the representative rattle-type structure can be observed clearly (as Fig.2**g** and Fig.2**h**). In addition, the distinct mesoporous opening structure can be observed after the removing of CTAB in the mesoporous silica shell (as Fig.2**h**).

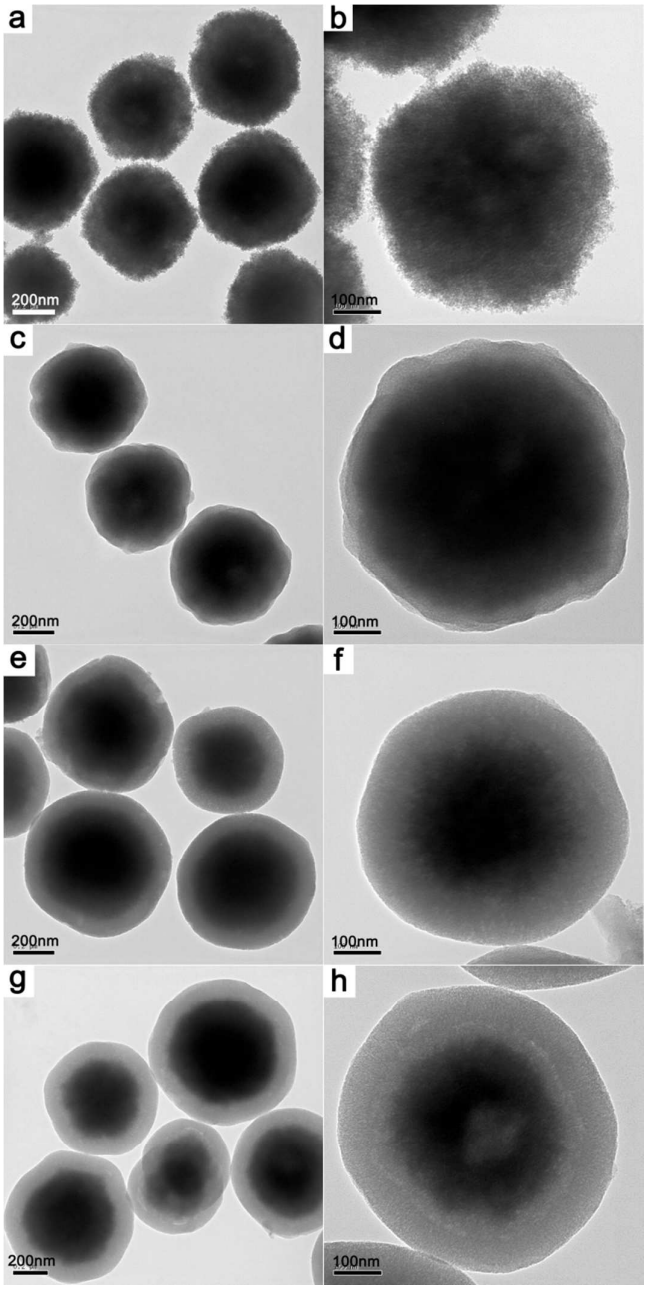

Fig.2 TEM images of Fe_3O_4 (**a** and **b**), Fe_3O_4@SiO_2 (**c** and **d**), Fe_3O_4@SiO_2@mSiO_2/CTAB (**e** and **f**) and R-Fe_3O_4@mSiO_2 (**g** and **h**).

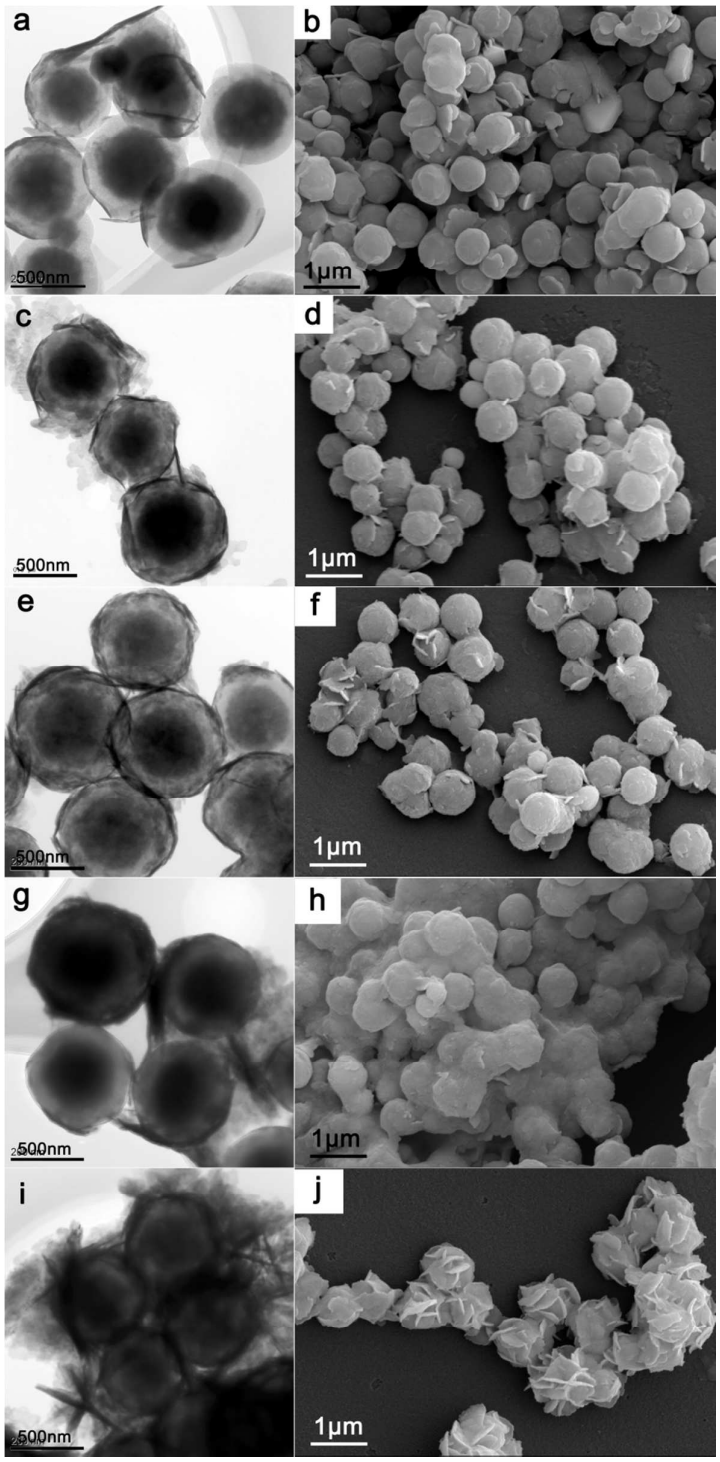

Fig.3 TEM and SEM images of the R-Fe_3O_4@mSiO_2@BiOBr hierarchical photocatalysts synthesized under the addition of $Bi(NO_3)_3 \cdot 5H_2O$: 0.2 g (**a** and **b**), 0.4 g (**c** and **d**), 0.6 g (**e** and **f**), 0.8 g (**g** and **h**) and 1.0 g (**i** and **j**). The addition content of PVP is 0.1 g, and the reaction time and reaction temperature is 4 h and 180℃, respectively.

Afterwards, the R-Fe_3O_4@mSiO_2 microspheres were modified by APTES, and the corresponding

FTIR characterization was provided. As shown as Fig.S1**a**, the characteristic absorption peaks corresponding to the antisymmetric and symmetric stretching vibration of Si-O-Si bond in oxygen-silicon tetrahedron can be clearly observed at 1077 and 793 cm^{-1}, respectively. And the characteristic absorption peak of Fe-O bond can also be observed at 480 cm^{-1}. After the amino-functionalization, the characteristic absorption peaks at 2918 and 2850 cm^{-1} corresponding to the symmetric and antisymmetric stretching vibrations of ν_{C-H} in methyl and methylene appeared (as Fig.S1**b**). Beyond that, a shoulder peak attributed to the stretching vibration of δ_{N-H} and γ_{N-H} can be observed clearly at 1552 cm^{-1}. It indicates that the R-Fe_3O_4@$mSiO_2$ microspheres had been successfully modified by APTES.

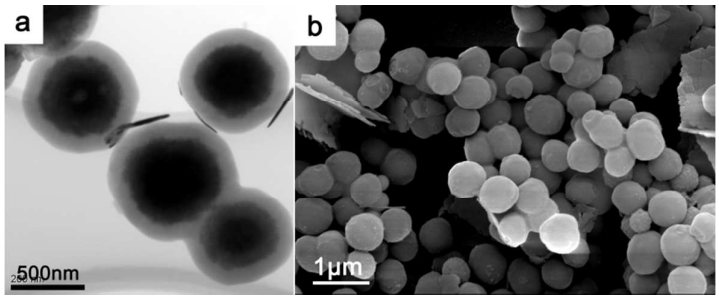

Fig.4 TEM and SEM images of the R-Fe_3O_4@$mSiO_2$@BiOBr hierarchical photocatalyst synthesized on the surface of magnetic R-Fe_3O_4@$mSiO_2$ microspheres which were not functionalized by APTES. The addition content of $Bi(NO_3)_3 \cdot 5H_2O$ and PVP is 1.0 g and 0.1 g, respectively. The reaction time and reaction temperature is 4 h and 180℃, respectively.

After the amino-functionalization, the BiOBr nanosheets were synthesized on the surface of the R-Fe_3O_4@$mSiO_2$ microspheres by the orienting role of the amino-groups. Subsequently, the reaction time was chosen as 4 h, and a series of R-Fe_3O_4@$mSiO_2$@BiOBr hierarchical photocatalysts were synthesized by adjusting the addition content of the bismuth source. After the assembly of the BiOBr nanosheets, the sheet structures, which is the BiOBr photocatalyst, can be observed clearly on the surface of the R-Fe_3O_4@$mSiO_2$ microspheres (as Fig.3**a-j**). Obviously, the amounts of BiOBr nanosheets on the surface of the R-Fe_3O_4@$mSiO_2$ microspheres would increase with the incease of the bismuth source from 0.2 g to 1.0 g. In particular, when the addition of the bismuth source was 1.0 g, the morphology of the R-Fe_3O_4@$mSiO_2$@BiOBr photocatalyst exhibited the representative hierarchical structure (as Fig.3**i** and Fig.3**j**). In addition, the assembly of the BiOBr nanosheets was also carried out on the surface of the magnetic R-Fe_3O_4@$mSiO_2$ microspheres which were not

functionalized by the APTES, and the corresponding TEM and SEM images were shown in Fig.4**a** and Fig.4**b**. Apparently, very few sheet structures can be observed on the surface of the R-Fe_3O_4@mSiO_2 microspheres, which indicates that the amino-groups on the surface of the magnetic R-Fe_3O_4@mSiO_2 microspheres indeed play an important role in the oriented growth of the BiOBr nanosheets. Predominantly, the amino-groups on the surface of the magnetic R-Fe_3O_4@mSiO_2 microspheres can chelate the Bi^{3+} ions in the synthesis system, which would produce the strong orientation effect for the growth of BiOBr nanosheets.

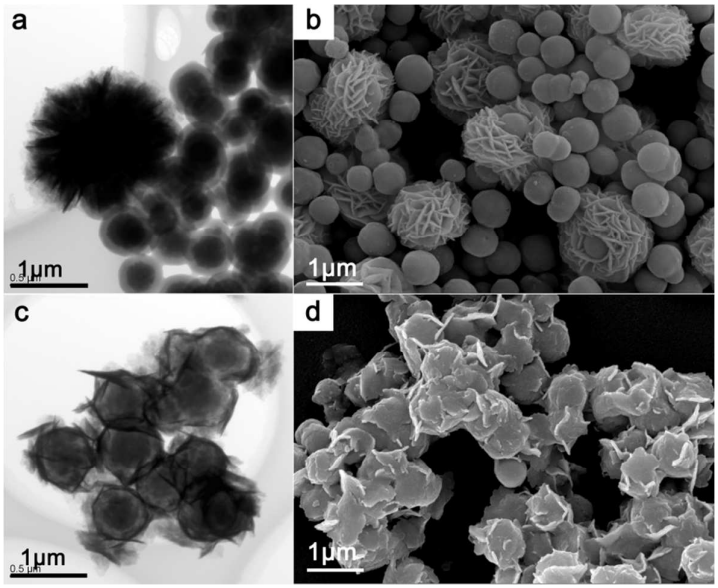

Fig.5 TEM and SEM images of the R-Fe_3O_4@mSiO_2@BiOBr hierarchical photocatalyst synthesized under the reaction of 2 h (**a** and **b**) and 6 h (**c** and **d**). The reaction temperature is 180℃, and the addition content of $Bi(NO_3)_3 \cdot 5H_2O$ and PVP is 1.0 g and 0.1 g, respectively.

Among that, the effect of reaction time was also investigated, and the corresponding TEM and SEM images were shown in Fig.5. When the reaction time was chosen as 2 h, the independent R-Fe_3O_4@mSiO_2 microspheres and BiOBr hierarchical photocatalyst would be observed (as Fig.5**a** and Fig.5**b**). However, when the reaction time was extended to 6 h, more BiOBr nanosheets would be synthesized on the surface of magnetic R-Fe_3O_4@mSiO_2 microspheres (as Fig.5**c** and Fig.5**d**). It indicates that the reaction time also plays an important role to the synthesis of the R-Fe_3O_4@mSiO_2@BiOBr hierarchical photocatalyst. In detail, the assembly of the BiOBr nanosheets on the surface of the amino-functionalized magnetic R-Fe_3O_4@mSiO_2 microspheres depends on the reaction time obviously. When the reaction time is very short, there is not enough time to support the assembly of the BiOBr nanosheets on the surface of the amino-functionalized

magnetic R-Fe_3O_4@$mSiO_2$ microspheres, so the R-Fe_3O_4@$mSiO_2$@BiOBr hierarchical photocatalyst can not be obtained, and only the independent magnetic R-Fe_3O_4@$mSiO_2$ microspheres and a small amount of BiOBr hierarchical photocatalyst can be obtained. Instead, when the reaction takes longer time, the bismuth source would be consumed entirely, and more BiOBr nanosheets would be assembled on the surface of amino-functionalized magnetic R-Fe_3O_4@$mSiO_2$ microspheres under the oriented effect of the surface amino-groups.

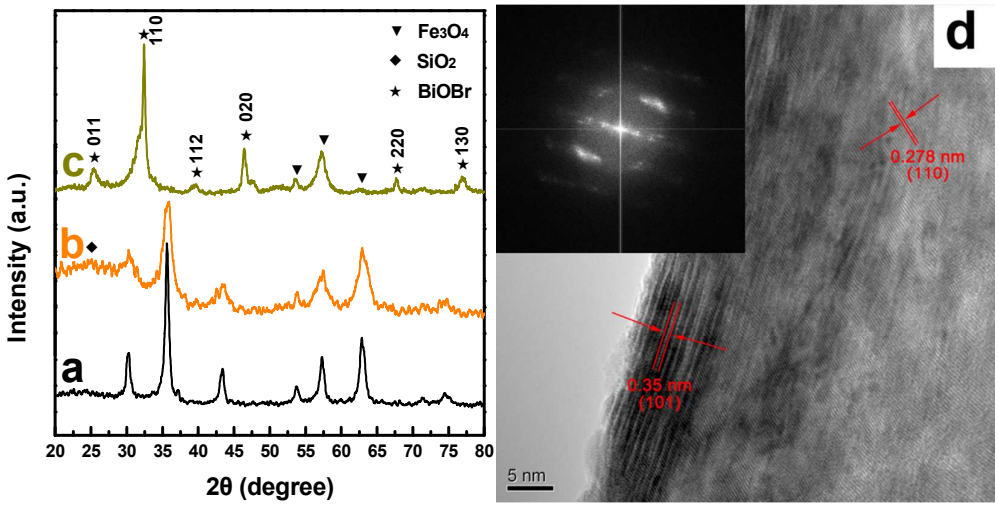

Fig.6 XRD patterns of Fe_3O_4 (**a**), R-Fe_3O_4@$mSiO_2$ (**b**) and R-Fe_3O_4@$mSiO_2$@BiOBr-1-4 (**c**), respectively. (**d**) HRTEM image of the R-Fe_3O_4@$mSiO_2$@BiOBr-1-4 hierarchical photocatalyst. The insert is the corresponding FFT image.

XPS spectra for the measurement of the surface compositions and chemical states of this R-Fe_3O_4@$mSiO_2$@BiOBr-1-4 hierarchical photocatalyst are displayed in Fig.S2, and the XPS spectrum in Fig.S2**a** reveals that the surface of this photocatalyst was consisted with O, C, Bi and Br. As shown as Fig.S2**b**, two peaks at 159.2 and 164.5 eV is respectively attributed to $Bi4f_{7/2}$ and $Bi4f_{5/2}$, which indicates the existence of Bi^{3+} in BiOBr. The $Br3d_{5/2}$ and $Br3d_{3/2}$ peaks (Fig.S2**c**) is associated with the binding energy at 68.4 and 69.4 eV, respectively. Two peaks at 531.5 eV and 530.1 eV should be fitted with the characteristic peaks of O1s in BiOBr, and two peaks at 533.7 eV and 532.8 eV should be assigned to the characteristic peaks of O1s in PVP and other components (such as -OH groups and crystalline H_2O) adsorbed on the surface of BiOBr photocatalyst (Fig.S2**d**). In addition, three peaks at 287.9 eV, 285.9 eV and 284.7 eV in Fig.S2**e** should be attributed to the characteristic peaks of C1s in PVP adsorbed on the surface of BiOBr photocatalyst. It had been well demonstrated that the BiOBr photocatalyst had been successfully assembled on the surface of the

R-Fe_3O_4@mSiO_2 microspheres.

The XRD was employed to determine the crystallographic phase of the products, and the corresponding XRD patterns were displayed in Fig.6. As shown as Fig.6**a**, the XRD pattern is well indexed to the standard cubic phase of Fe_3O_4 (JCPDS 65-3107). Fig.6**b** shows that a wide diffraction peak around 24º corresponding to the amorphous silica can be observed after the introduction of mesoporous silica. Subsequently, six intense and sharp diffraction peaks at 25.3, 32.5, 39.6, 46.4, 67.7 and 77.0 º indexed to the tetragonal phase of BiOBr can be observed clearly (Fig.6**c**), indicating that the BiOBr nanosheets assembled on the surface of the amino-functionlized R-Fe_3O_4@mSiO_2 microspheres are well-crystallized. In addition, Fig.6**d** dispalys the high resolution image of the R-Fe_3O_4@mSiO_2@BiOBr-1-4 hierarchical photocatalyst, the lattice fringes with d-spacing of 0.278 nm and 0.35 nm can be assigned to the (110) and (101) lattice planes of the tetragonal system of BiOBr, respectively. In addition, the FFT image in insert of Fig.6**d** can also demonstrate aforementioned conclusion.

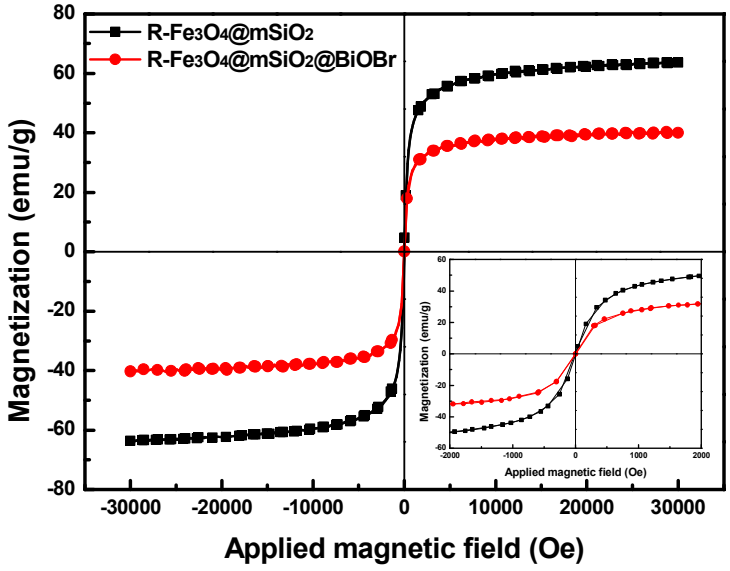

Fig.7 Magnetization curves of R-Fe_3O_4@mSiO_2 (**a**) and R-Fe_3O_4@mSiO_2@BiOBr-1-4 (**b**) measured at room temperature, and the insert is the corresponding magnetization of the low field (-2000~2000 Oe).

It is important to characterize the magnetic properties of the magnetic materials. Fig.7 displays the VSM curves of R-Fe_3O_4@mSiO_2 microspheres and R-Fe_3O_4@mSiO_2@BiOBr-1-4 hierarchical photocatalyst. It is easy to see that the saturation magnetization of aforementioned two materials is about 63 and 40 emu/g, respectively. For the assembly of BiOBr nanosheets on the surface of R-Fe_3O_4@mSiO_2 microspheres, the corresponding saturation magnetization had decreased to some

extent. However, it can still fulfill the simple separation of the photocatalyst from the degradation system. In addition, the magnification of the low fields (in the insert) shows that both magnetic particles exhibit the representative feature of superparamagnetism for no hysteresis is observed in the low fields, which would be very conducive to the redispersion of the particles.

3.2 Photocatalytic Performance

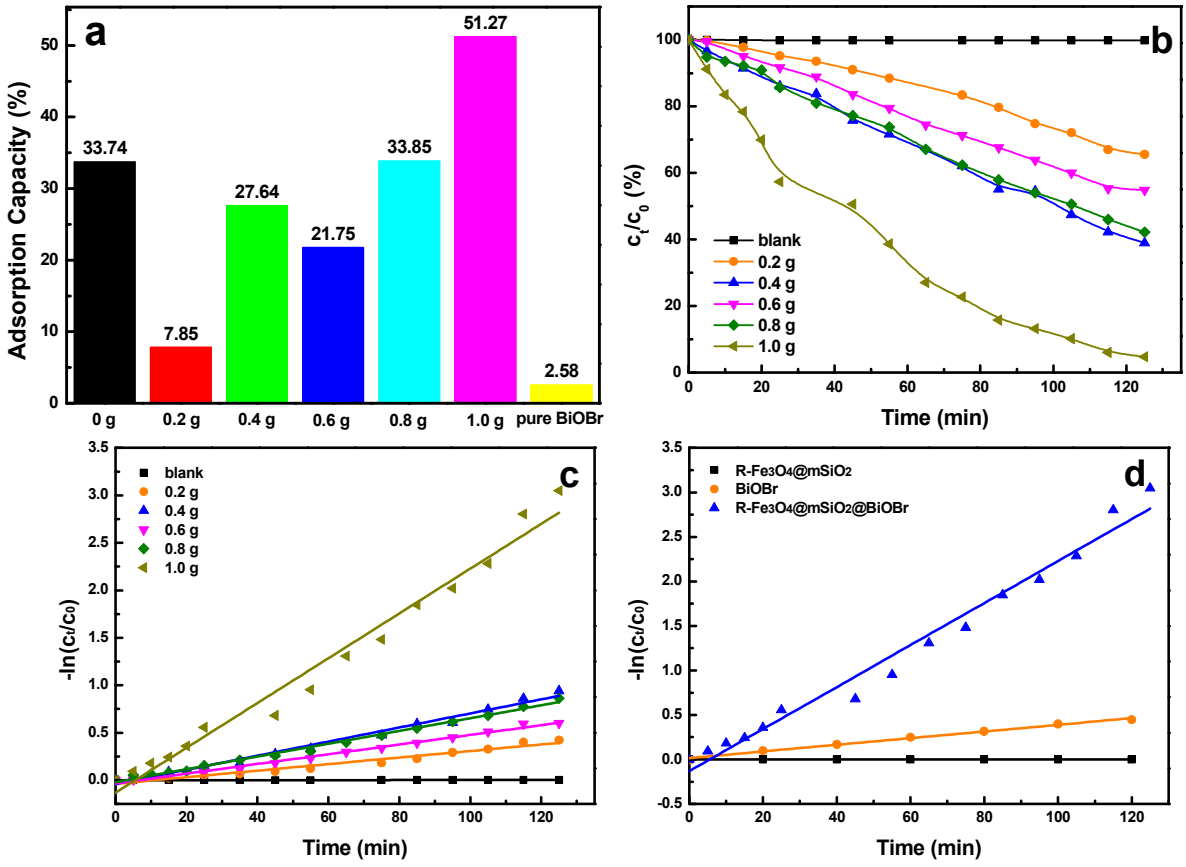

Fig.8 The saturated adsorptions in dark (**a**), the photodegradation kinetic curves of the photocatalysts with different BiOBr assembly (**b**), the corresponding fitted kinetic curves according to the Langmuir-Hinshelwood model (**c**) and the Langmuir-Hinshelwood model of the photoactivity of R-Fe_3O_4@$mSiO_2$, pure BiOBr and R-Fe_3O_4@$mSiO_2$@BiOBr-1-4 (**d**).

The photodegradation of MB under visible-light response (λ > 420 nm) was used as a probe to evaluate the performance of the R-Fe_3O_4@$mSiO_2$@BiOBr photocatalysts. Firstly, these photocatalysts prepared under different addition content of bismuth source and the pure BiOBr photocatalyst were kept for 30 min in dark under vigorous agitation, and the corresponding saturated adsorption capacities were displayed in Fig.8**a**. Obviously, the saturated adsorption capacity of the photocatalyst to MB improved gradually with increasing the bismuth source except the

R-Fe_3O_4@mSiO_2@BiOBr-0.4-4 (~27.64 %), and R-Fe_3O_4@mSiO_2@BiOBr-1-4 photocatalyst exhibited the highest saturated adsorption capacity (~51.27 %) to MB, which may be resulted from the increased BiOBr assembly on the surface of the magnetic R-Fe_3O_4@mSiO_2 microspheres. In addition, the saturated adsorption abilities of the pure BiOBr photocatalyst and R-Fe_3O_4@mSiO_2 microspheres is respectively about 2.58% and 33.74%, which indicates that pure BiOBr exhibits the poor adsorption ability to MB molecules, but R-Fe_3O_4@mSiO_2 microspheres show the superior adsorption ability to MB molecules for the existence of the ordered mesoporous structure and the inner cavities. At the same time, it indicates that the introduction of the R-Fe_3O_4@mSiO_2 microspheres with the unique structure had indeed enhanced the adsorption ability of the BiOBr photocatalyst. Subsequently, the photodegradation of MB was initiated under visible-light response, and the corresponding photodegradation kinetic curves were displayed in Fig.8**b**. Then, the degradation kinetics of MB were also investigated by fitting the experimental data to the Langmuir-Hinshelwood models following the equation: $-ln(c_t/c_o)=kt$ (Fig.8**c**). Obviously, all the photodegradations of MB by R-Fe_3O_4@mSiO_2@BiOBr-α-4 photocatalysts obeyed the first order kinetics well. It is easy to see that the photoactivities of these photocatalysts are basically consistent with their adsorption capacity. Among them, the R-Fe_3O_4@mSiO_2@BiOBr-1-4 photocatalyst, which exhibited the highest photoactivity ($k = 0.0223\ min^{-1}$), and about 96% of MB molecules was degraded within 120 min. However, it is basically the same between R-Fe_3O_4@mSiO_2@BiOBr-0.4-4 ($k = 0.0070\ min^{-1}$) and R-Fe_3O_4@mSiO_2@BiOBr-0.8-4 ($k = 0.0064\ min^{-1}$). As a whole, the increase of the bismuth source would lead to the increased effective contact area with MB molecules for the increased assembly of the BiOBr nanosheets on the amino-functionalized magnetic R-Fe_3O_4@mSiO_2 microspheres, correspondingly, it would lead to the higher adsorption capacity and enhanced photoactivity. Beyond that, the R-Fe_3O_4@mSiO_2 microspheres and pure BiOBr photocatalyst were chosen as the reference photocatalysts, and the corresponding photoactivities were also investigated by catalyzing the degradation of MB in water system. Fig.8**d** displays the corresponding Langmuir-Hinshelwood models of the photodegradation kinetic curves, and it shows that the R-Fe_3O_4@mSiO_2 microspheres do not exhibit the photodegradation ability to MB under visible-light irradiation. Obviously, the photoactivity of the R-Fe_3O_4@mSiO_2@BiOBr-1-4 hierarchical photocatalyst is far higher (about 5.9 times) than that of the pure BiOBr photocatalyst. It indicates that the introduction of the rattle-type magnetic mesoporous Fe_3O_4@mSiO_2 microspheres with

unique structure had indeed enhanced the photoactivity of the BiOBr photocatalyst significantly, which should mainly caused by the superior adsorption ability to the MB molecules and the fast interfacial charge transfer (Fig.S3).

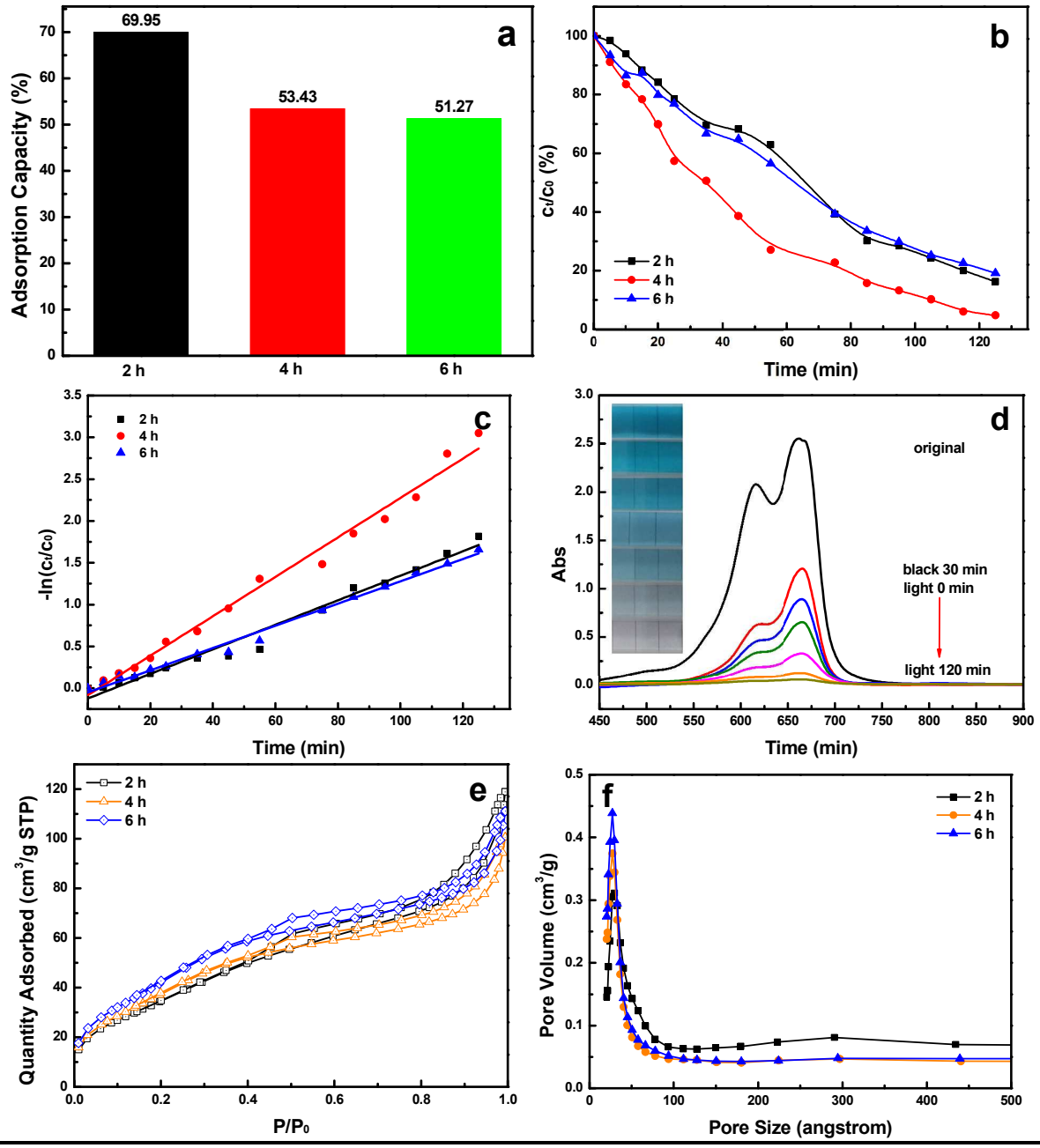

Sample	BET surface area (m^2/g)	Pore size (nm)	Saturated adsorption capacity (%)	Rate constant (min^{-1})
R-Fe_3O_4@mSiO_2@BiOBr-1-2	131.66	55	69.95	0.0135
R-Fe_3O_4@mSiO_2@BiOBr-1-4	143.78	46	53.43	0.0223
R-Fe_3O_4@mSiO_2@BiOBr-1-6	161.96	44	51.27	0.0128

Fig.9 The saturated adsorptions in dark (**a**), the photodegradation kinetic curves of the photocatalysts prepared

under the different reaction time (**b**), the fitted kinetic curves according to the Langmuir-Hinshelwood model (**c**) and the corresponding UV-vis spectra of MB solution under the catalysis of the R-Fe_3O_4@$mSiO_2$@BiOBr-1-4 hierarchical photocatalyst (**d**). The inset is the corresponding digital photos of the photodegradation system. The N_2 adsorption/desorption isotherms (**e**) and pore size distribution (**f**) of the samples, and the table is the summary of the whole data.

Furthermore, the saturated adsorptions and photoactivities of the R-Fe_3O_4@$mSiO_2$@BiOBr hierarchical photocatalysts synthesized under the different reaction time (2 h, 4 h and 6 h) were also investigated. Fig.9**a** displays the saturated adsorption capacities of the R-Fe_3O_4@$mSiO_2$@BiOBr-1-2, R-Fe_3O_4@$mSiO_2$@BiOBr-1-4 and R-Fe_3O_4@$mSiO_2$@BiOBr-1-6, and it shows that both of R-Fe_3O_4@$mSiO_2$@BiOBr-1-2 and R-Fe_3O_4@$mSiO_2$@BiOBr-1-4 exhibits higher adsorption capacity than that of the R-Fe_3O_4@$mSiO_2$@BiOBr-1-6, and the R-Fe_3O_4@$mSiO_2$@BiOBr-1-2 photocatalyst shows the highest saturated adsorption (~69.95 %) among three photocatalysts. To explain this phenomenon, these three materials were characterized by N_2 adsorption/desorption, and Fig.9**e** and Fig.9**f** displays the corresponding isotherms and pore size distributions. Beyond that, the summary of all data was also displayed in the table of Fig.9. Although the BET surface area of R-Fe_3O_4@$mSiO_2$@BiOBr-1-2 is the smallest one (about 131.66 m^2/g), the independent existence of the BiOBr hierarchical microparticles and R-Fe_3O_4@$mSiO_2$ microspheres (as Fig.5**a** and Fig.5**b**) would exhibit higher adsorption ability to the MB molecules for the combined effect of the BiOBr surface and the orderly mesoporous opening structure of the R-Fe_3O_4@$mSiO_2$ microspheres. Subsequently, the adsorption ability of the R-Fe_3O_4@$mSiO_2$@BiOBr photocatalyst would gradually decrease with the prolonging of the reaction time, which is caused by the sacrificial effect of the orderly mesoporous opening structure of the R-Fe_3O_4@$mSiO_2$ microspheres for the increased assembly of BiOBr nanosheets. Furthermore, it also indicates that the orderly mesoporous opening structure of the R-Fe_3O_4@$mSiO_2$ microspheres plays an important role to the enhanced adsorption ability. Fig.9**b** and Fig.9**c** display the corresponding photocatalytic degradation kinetic curves and the Langmuir-Hinshelwood models, it is noteworthy that the R-Fe_3O_4@$mSiO_2$@BiOBr-1-4 hierarchical photocatalyst exhibited the highest photoactivity during 120 min, and it was lower for R-Fe_3O_4@$mSiO_2$@BiOBr-1-2 (~84%, $k = 0.0135\ min^{-1}$) and R-Fe_3O_4@$mSiO_2$@BiOBr-1-6 (~81%, $k = 0.0128\ min^{-1}$). Considering the BET surface area (as the table in Fig.9), it would gradually increase (131.66 to 161.96 m^2/g) with the prolonging of the reaction time. When the reaction time is

2 h, the photodegradation of MB is mainly caused by the independent BiOBr hierarchical microparticles, so its photoactivity is lower than that of R-Fe_3O_4@mSiO_2@BiOBr-1-4 hierarchical photocatalyst. When the reaction time is 6 h, the mass transfer effect of the orderly mesoporous opening structure of the R-Fe_3O_4@mSiO_2 microspheres would be weakened significantly by the excess assembly of BiOBr nanosheets, thus its photoactivity is also lower than that of R-Fe_3O_4@mSiO_2@BiOBr-1-4 hierarchical photocatalyst even its BET surface area is higher. When the reaction time is 4 h, the mass transfer effect of the orderly mesoporous opening structure of the R-Fe_3O_4@mSiO_2 microspheres would not be inhibited for the reasonable assembly of BiOBr nanosheets, so the R-Fe_3O_4@mSiO_2@BiOBr-1-4 hierarchical photocatalyst exhibits the highest photoactivity. Fig.9**d** displays the corresponding UV-vis spectra of MB solution at the presence of R-Fe_3O_4@mSiO_2@BiOBr-1-4 hierarchical photocatalyst under visible-light irradiation, and it shows that the maximum absorption peak (662 nm) would gradually weaken with the prolonging of the illumination time and would disappear entirely after being irradiated for 120 min, indicating that the MB molecules had been degraded entirely. At the same time, the digital photos in the inset of Fig.9**d** also demonstrate above conclusion. After the photocatalytic degradation process, the R-Fe_3O_4@mSiO_2@BiOBr-1-4 hierarchical photocatalyst was also characterized by the TEM instrument, and the corresponding TEM and HRTEM images were displayed in Fig.S4**a** and Fig.S4**b**. Both of the images shows unobvious variation, indicating that this novel hierarchical photocatalyst exhibits superior stability.

3.3 Photocatalytic Mechanism

In order to investigate the main active species involved in MB photodegradation over the R-Fe_3O_4@mSiO_2@BiOBr hierarchical photocatalyst, KI, TBA, IPA and BQ was used as the scavenger of photogenerated holes (h^+), photoexcited electrons (e^-), hydroxyl radicals (▪*OH*) and superoxide radicals ($O_2^{\bullet-}$), respectively. As shown in Fig.10, when KI or BQ was added into the degradation system, the significant decrease in photoactivity would be obtained, and the corresponding degradation rate is about 54% and 61% during 120 min, respectively. Compared with that of the degradation system which do not contain any scavenger, it demonstrates that both the h^+ and $O_2^{\bullet-}$ radicals are the main active species. However, when TBA or IPA was added into the degradation system, the change of the photoactivity would be not obvious, indicating that the e^- and ▪*OH* radicals are not the main active species. Therefore, in this photocatalytic degradation system,

the possible photocatalytic mechanism are proposed as:

$$photocatalyst + h\nu \rightarrow photocatalyst\ (h^+ + e^-) \quad (1)$$

$$O_2 + e^- \rightarrow O_2^{\bullet -} \quad (2)$$

$$O_2^{\bullet -} + 2H^+ + e^- \rightarrow H_2O_2 \quad (3)$$

$$H_2O_2 + e^- \rightarrow \bullet OH + OH^- \quad (4)$$

$$OH^- + h^+ \rightarrow \bullet OH \quad (5)$$

$$H_2O + h^+ \rightarrow \bullet OH + H^+ \quad (6)$$

$$MB + h^+ \rightarrow MB^+ \quad (7)$$

$$MB^+ + O_2^{\bullet -} \rightarrow degradation\ products \quad (8)$$

$$MB + \bullet OH \rightarrow degradation\ products \quad (9)$$

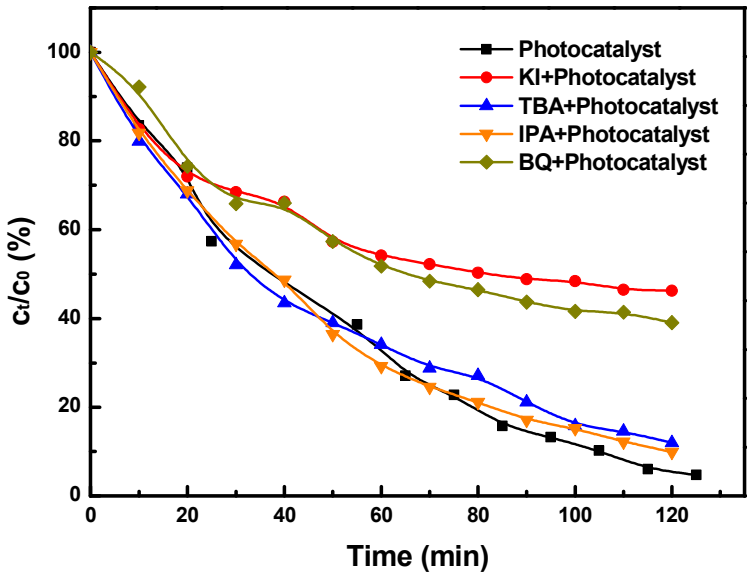

Fig.10 Effects of different scavengers on degradation of MB in the presence of R-Fe_3O_4@mSiO_2@BiOBr-1-4 hierarchical photocatalyst under visible-light irradiation.

Under visible-light irradiation, the reaction is initiated with the excitation of the photocatalyst, resulting in the promotion of electrons (*e*-) from the valence band (VB) to the conduction band (CB) of the BiOBr semiconductor and the generation of holes (*h*+) in the VB (Eqs.(1)). Then, the e^- react with O_2 molecules to generate $O_2^{\bullet -}$ radicals (Eqs.(2)), and $O_2^{\bullet -}$ radicals can react with H^+ ions and e^- to generate H_2O_2 molecules (Eqs.(3)). Subsequently, H_2O_2 molecules react with e^- to generate $\bullet OH$ radicals and OH^- ions (Eqs.(4)). Simultaneously, OH^- ions react with h^+ to generate $\bullet OH$ radicals (Eqs.(5)), and H_2O molecules react with h^+ to generate $\bullet OH$ radicals and H^+ ions (Eqs.(6)). Beyond that, MB can react with h^+ to generate the activated MB^+ (Eqs.(7)), then activated MB^+ react

with $O_2^{\bullet-}$ radicals to generate the ultimate degradation products (H_2O and CO_2) (Eqs.(8)). At the same time, MB can also directly react with $\cdot OH$ radicals to generate the ultimate degradation products (Eqs.(9)). According to the radicals trapping experiments, the h^+ and $O_2^{\bullet-}$ radicals are the main active species, so the Eqs.(1), (2), (7) and (8) are the main degradation routes.

4. Conclusion

In this paper, a novel rattle-type magnetic mesoporous Fe_3O_4@mSiO_2@BiOBr hierarchical photocatalyst was successfully synthesized by a facile solvothermal synthesis under the orientation of the surface amino-groups of rattle-type magnetic mesoporous Fe_3O_4@mSiO_2 microspheres. Due to the presence of inner cavity and orderly mesoporous opening structure, this novel photocatalyst exhibits superior adsorption and transfer performance to organic contaminants in water system. Especially, the complex between BiOBr and SiO_2 had significantly increased the absorption ability to visible-light to some extent for the direct contact of the interfaces of two materials. Research shows that the assembly capacity of BiOBr plays an important role to the enhanced photoactivity. Even though methylene blue is a relatively stable organic contaminant, it can still be decomposed completely by this novel photocatalyst within a very short time (about 120 min). Encouragingly, the photoactivity of this novel photocatalyst is far higher (about 2.6 times) than that of pure BiOBr photocatalyst for its unique structure. According to the radical trapping experiments, the photogenerated holes (h+) and superoxide radicals ($O_2^{\bullet-}$) were considered as the main active species to drive the photodegradation under visible-light irradiation. For the unique structures and fast interfacial charge transfer, this novel photocatalyst absolutely is a superior alternative visible-light-driven photocatalyst.

Acknowledgment

The authors are grateful for the financial support provided by the National Natural Science Foundation of China (No. 51173146 and NO. 21201140), basic research fund of Northwestern polytechnical university (3102014JCQ01094, 3102014ZD).

References

[1] X. Dang, X. Zhang, W. Zhang, X. Dong, G. Wang, C. Ma, X. Zhang, H. Ma and M. Xue. Ultra-thin C_3N_4 nanosheets for rapid charge transfer in the core-shell heterojunction of a-sulfur@C_3N_4 for superior metal-free photocatalysis under visible light. *RSC. Adv*. 2015, 5, 15052–

15058.

[2] S. Liu, M.-Q. Yang and Y.-J. Xu. Surface charge promotes the synthesis of large, flat structured graphene-(CdS nanowire)-TiO_2 nanocomposites as versatile visible light photocatalysts. *J. Mater. Chem. A* 2014, 2, 430–440.

[3] X. Ren, P. Ying, Z. Yang, M. Shang, H. Hou and F. Gao. Foaming-assisted electrospinning of large-pore mesoporous ZnO nanofibers with tailored structures and enhanced photocatalytic activity. *RSC. Adv*. 2015, 5, 16361–16367.

[4] L. J. Zhang, R. Zheng, S. Li, B. K. Liu, D. J. Wang, L. L. Wang, and T. F. Xie. Enhanced Photocatalytic H_2 Generation on Cadmium Sulfide Nanorods with Cobalt Hydroxide as Cocatalyst and Insights into Their Photogenerated Charge Transfer Properties. *ACS Appl. Mater. Interfaces* 2014, 6, 13406−13412.

[5] J. Jiang, L. Tong, H. Zhou, F. Zhang, J. Ding, D. Zhang and T. Fan. A photochromic nano-system via self-recovery for stable photocatalytic hydrogen evolution by optimizing TiO_2 surface energy. *RSC. Adv*. 2015, 5, 15844–15849.

[6] S. Weng, Z.X. Pei, Z. Zheng, J. Hu, and P. Liu. Exciton-Free, Nonsensitized Degradation of 2-Naphthol by Facet-Dependent BiOCl under Visible Light: Novel Evidence of Surface-State Photocatalysis. *ACS Appl. Mater. Interfaces* 2013, 5, 12380−12386.

[7] X. Shi, X. Chen, X. Chen, S. Zhou, S. Lou , Y. Wang, L. Yuan. PVP assisted hydrothermal synthesis of BiOBr hierarchical nanostructures and high photocatalytic capacity. *Chem. Eng. J*. 2013, 222, 120–127.

[8] C. Yu, F. Cao, G. Li, R. Wei, J. C. Yu, R. Jin, Q. Fan, C. Wang. Novel noble metal (Rh, Pd, Pt)/BiOX(Cl, Br, I) composite photocatalysts with enhanced photocatalytic performance in dye degradation. *Sep. Purif. Technol*. 2013, 120, 110–122.

[9] G. Jiang, R. Wang, X. Wang, X. Xi, R. Hu, Y. Zhou, S. Wang, T. Wang, and W. Chen. Novel Highly Active Visible-Light-Induced Photocatalysts Based on BiOBr with Ti Doping and Ag Decorating. *ACS Appl. Mater. Interfaces* 2012, 4, 4440−4444.

[10] Xian-Xian Wei, Cheng-Meng Chen, Shao-Qing Guo, Fang Guo, Xiao-Ming Li, Xiao-Xiao Wang, Hai-Tao Cui, Liang-Fu Zhao and Wen Li. Advanced visible-light-driven photocatalyst BiOBr-TiO_2-graphene composite with graphene as a nano-filler. *J. Mater. Chem. A* 2014, 2, 4667–4675.

[11] L. Zhang, W. Wang, S. Sun, Y. Sun, E. Gao, Z. Zhang. Elimination of BPA endocrine disruptor by magnetic BiOBr@SiO_2@Fe_3O_4 photocatalyst. *Appl. Catal. B-Environ*. 2014, 148, 164–169.

[12] J.-F. Guo, B. Ma, A. Yin, K. Fan, W.-L. Dai. Photodegradation of rhodamine B and 4-chlorophenol using plasmonic photocatalyst of Ag-AgI/Fe_3O_4@SiO_2 magnetic nanoparticle under visible light irradiation. *Appl. Catal. B-Environ*. 2011, 101, 580–586.

[13] H.-S. Huang, K.-H Chang, N. Suzuki, Y. Yamauchi, C.-C. Hu and K. C.-W. Wu. Evaporation-Induced Coating of Hydrous Ruthenium Oxide on Mesoporous Silica Nanoparticles to Develop High-Performance Supercapacitors. *Small*. 2013, 9, 2520–2526.

[14] J. T. Lee, Y. Zhao, S. Thieme, H. Kim, M. Oschatz, L. Borchardt, A. Magasinski, W.-I. Cho, S. Kaskel and G. Yushin. Sulfur-Infiltrated Micro- and Mesoporous Silicon Carbide-Derived Carbon Cathode for High-Performance Lithium Sulfur Batteries. *Adv. Mater*. 2013, 25, 4573–4579.

[15] W. Li, B. Zhang, X. Li, H. Zhang, Q. Zhang. Preparation and characterization of novel immobilized Fe_3O_4@SiO_2@mSiO_2-Pd(0) catalyst with large pore-size mesoporous for Suzuki coupling reaction. *Appl. Catal. A-Gen*. 2013, 459, 65–72.

[16] J. Di, J. Xia, S. Yin, H. Xu, L. Xu, Y. Xu, M. He and H. Li. Preparation of sphere-like g-C3N4/BiOI photocatalystsviaa reactable ionic liquid for visible-light-driven photocatalytic degradation of pollutants. *J. Mater. Chem. A* 2014, 2, 5340–5351.

[17] F. Li, Q. Wang, J. Ran, Y. Hao, X. Wang, D. Zhao and S. Z. Qiao. Ionic liquid self-combustion synthesis of BiOBr/$Bi_{24}O_{31}Br_{10}$ heterojunctions with exceptional visible-light photocatalytic performances. *Nanoscale* 2015, 7, 1116–1126.

[18] L. Ye, J. Liu, Z. Jiang, T. Peng, L. Zan. Facets coupling of BiOBr-g-C_3N_4 composite photocatalyst for enhanced visible-light-driven photocatalytic activity. *Appl. Catal. B-Environ*. 2013, 142, 1–7.

[19] X. Wang, W. Yang, F. Li, Y. Xue, R. Liu, and Y. Hao. In Situ Microwave-Assisted Synthesis of Porous N-TiO_2/g-C_3N_4 Heterojunctions with Enhanced Visible-Light Photocatalytic Properties. *Ind. Eng. Chem. Res*. 2013, 52, 17140−17150.